Developmental Biology **232,** 458–470 (2001)
doi:10.1006/dbio.2001.0189, available online at http://www.idealibrary.com on IDEAL®

Three-Dimensional Digital Mouse Atlas Using High-Resolution MRI

Marc Dhenain,[1] Seth W. Ruffins, and Russell E. Jacobs[2]

Division of Biology, Biological Imaging Center, Beckman Institute, California Institute of Technology, Pasadena, California 91125

We present an archetypal digital atlas of the mouse embryo based on microscopic magnetic resonance imaging. The atlas is composed of three modules: (1) images of fixed embryos 6 to 15.5 days postconception (dpc) [Theiler Stages (TS) 8 to 24]; (2) an annotated atlas of the anterior portion of a 13.5 dpc (TS 22) mouse with anatomical structures delineated and linked to explanatory files; and (3) three-dimensional renderings of the entire 13.5 dpc embryo and specific organ systems. The explanatory files include brief descriptions of the structure at each volume element in the image and links to 3D reconstructions, allowing visualization of the shape of the isolated structures. These files can also contain or be linked to other types of information and data including detailed anatomical and physiological information about structures with pointers to online references, relationships between structures, temporal characteristics (cell lineage patterns, size, and shape changes), and gene expression patterns (both spatial and temporal). As an example, we have "painted" in the expression pattern of Dlx5/Dlx6 genes. This digital atlas provides a means to put specific data within the context of normal specimen anatomy, to analyze the information in 3D, and to examine relationships between different types of information.

Key Words: **anatomy; brain; embryo; development; Dlx5/Dlx6; gene expression pattern; imaging; microscopy; mouse; MRI.**

INTRODUCTION

Anatomical atlases provide precise information about intricate organisms. Atlases are critical as analytical tools and for communicating complex information. Because data go beyond simple structural identification, the need arises for four-dimensional atlases that have the ability to incorporate additional information and that are extensible to high dimensions. The advent of inexpensive computers coupled with increasing speed and convenience in transporting large amounts of data have brought about changes in the way atlases are constructed and used. Digital media are making it feasible to construct a new generation of interactive atlases that link nomenclature directly with graphical plates (Brune *et al.*, 1999; Gibaud *et al.*, 1997; Williams and Doyle, 1996). These allow the visualization of complex three-dimensional (3D) structures, providing a better understanding of the geometry and spatial relationships between organ systems within the embryo (Kaufman *et al.*, 1997; Toga *et al.*, 1995). Further, these allow the user to "section" the digital specimen in any direction or angle. Thus, sections from one's own arbitrarily sliced sample may be directly compared with the same oblique sections from the digital atlas. Moreover, 3D representations make detailed morphometric measurements (distances, angles, surface areas, volumes) straightforward. Finally, with digital atlases, one can amalgamate spatial and temporal information from different experimental techniques into a single concise framework. For example, digital atlases can incorporate data regarding gene expression patterns (Ringwald *et al.*, 1999, 2000), chemoarchitectonic information, such as location of neurotransmitters (Jacobowitz and Abbott, 1998), receptor domains (Durstewitz *et al.*, 1999; Palermo-Neto, 1997), axonal projections, cell lineage and migration patterns, and the distribution of extracellular matrix components.

Recently a digital atlas of the embryonic mouse was generated from specimens processed by classic histological techniques (Brune *et al.*, 1999; Kaufman *et al.*, 1998). The

[1] Present address: Curie Institute–INSERM U350, Centre Universitaire Bat 112, 91405 Orsay Cedex, France.
[2] To whom correspondence should be addressed. Fax: (626) 449-5163. E-mail: rjacobs@caltech.edu.

0012-1606/01 $35.00

TABLE 1
Theiler Stage (TS)/Days Postconception (dpc) Conversion

TS	8	10	15	19	22	24
dpc	6	7	9.5	11.5	13.5	15.5

major drawback to this approach is that the specimen must be physically deconstructed from its native three dimensions into a series of two-dimensional (2D) sections. Each section is digitized and the images are reconstructed back into three dimensions. Artifacts generated during the physical processing of the sample (i.e., compression, shrinkage, tearing, folding, etc.) must be corrected with warping algorithms prior to reconstruction. Correcting and aligning sections is a nontrivial effort (Brune *et al.*, 1999; Kaufman *et al.*, 1998; Toga, 1998; Toga *et al.*, 1996; Toh *et al.*, 1996).

Magnetic resonance imaging microscopy (μMRI) is a qualitatively different imaging method that is able to distinguish soft tissues within optically opaque specimens. During a μMRI experiment, 3D data are collected directly from the intact specimen; thus, no artifacts are introduced by the physical deconstruction of the specimen. This noninvasive method offers several different sources of contrast and makes it possible to repeatedly image the same specimen over time (Jacobs and Fraser, 1994; Narasimhan and Jacobs, 1996a; Smith *et al.*, 1998). It can be used to image live or intact fixed samples. With this technique, the challenge is to obtain sufficient spatial resolution with sufficient contrast to differentiate anatomical features within the embryo. In practice, spatial resolution is limited by the intrinsically low intensity of the magnetic resonance signal (Callaghan, 1991b). Several groups have demonstrated near-cellular resolution using high magnetic field strengths, electronics optimized for small samples, and a variety of imaging protocols (Bowtell *et al.*, 1995; Narasimhan *et al.*, 1994; Johnson *et al.*, 1997).

In this study we present a digital atlas of the mouse embryo based on μMR imaging techniques. The atlas is composed of three different modules. First, it contains unprocessed μMR images of fixed embryos aged 6 to 15.5 days postconception (dpc) [Theiler Stages (TS) 8 to 24. See Table 1 for dpc to TS conversion]. Stacks of images can be viewed as transverse, horizontal, and sagittal movies. With appropriate software, the data may be rendered as volumes or sectioned at arbitrary orientations. Second, it contains an annotated atlas of the anterior portion of a 13.5 dpc (TS 22) mouse. In this atlas, anatomical structures in transverse sections of the embryo have been outlined. Each outlined structure is linked to a descriptive file using a weblet application. The explanatory files are also linked to 3D reconstructions allowing 3D visualization of the shape of the structures. Finally, the atlas contains a 3D rendering of the 13.5 dpc embryo. The whole embryo or specific organs (e.g., heart, liver, kidneys) can be displayed as 3D colored objects. As an example of how other types of information can be incorporated into this model, we have "painted" in the gene expression pattern of the Dlx5/Dlx6 genes that are involved in the regulation of forebrain development (Zerucha *et al.*, 2000). The digital atlas is presented as a Website (http://mouseatlas.caltech.edu).

MATERIALS AND METHODS

Animals

Mouse embryos aged 6 to 15.5 dpc (TS 8 to 24) were obtained from BDF1 females mated in the evening with BDF1 males. By convention, the morning on which the vaginal plug was found is referred to as 0.5 days postconception (Kaufman, 1994). We removed the embryos from pregnant females euthanized with CO_2. They were fixed by immersion in 4% paraformaldehyde in 0.1 M phosphate-buffered saline (PBS; pH = 7.4) for 24 h at 4°C, then washed several times in PBS. Thereafter, embryos were maintained at 4°C in 0.5% sodium azide PBS solution until imaged. For imaging, the fixed embryos were embedded in 1% agarose gels doped with magnetite or in fluorocarbon (Fluorinert), to minimize the signal intensity from media surrounding the embryo.

MR Imaging

Magnetic resonance imaging was performed at 4°C using an 11.7 Tesla, vertical bore (89-mm) Bruker AMX500 microimaging system (Bruker Instruments, Billerica, MA). We used an Acustar shielded gradient set (max 100 gauss/cm gradient strength) with home-built RF probes and low-noise preamplifier. Images used to create the atlas were recorded using 3D multispin echo protocols (one to eight echoes) with a data matrix of 256 × 128 × 128 points. Typical spatial resolution was 20 to 80 μm per voxel, depending on the size of the embryo. The images displayed in the atlas were padded with zeros to double the number of time domain points in each dimension, then Fourier transformed to yield a matrix of 512 × 256 × 256. This procedure is commonly called "zero-filling" and is a well-known interpolation method (Farrar and Becker, 1971; Fukushima and Roeder, 1981). In the case of 13.5 and 15.5 dpc (TS 22 and 24) embryos, T_2-weighted images were recorded using 3D multispin echo protocols [T_R = 1750 ms, T_E = 25 to 200 ms, bandwidth (BW) = 25 kHz, and number of averages (Na) = 4, acquisition time 36 h]. An additional set of T_2-weighted images (T_R = 3900 ms, T_E = 25 to 200 ms, BW = 25 kHz, and Na = 2, acquisition time 37 h) were recorded for the 13.5 dpc embryo. We note that the contrast is better for the 13.5 dpc embryo in T_2-weighted images (very long T_R and long T_E) than in T_1-weighted images (long T_R and short T_E). For other stages, several T_1-weighted images were recorded (T_R = 1000 ms, T_E = 5.5 to 27.5 ms, BW = 100 kHz, and Na = 4, acquisition time 18 h). (See Appendix for more information about details of MRI nomenclature and methodology.)

Website Creation and Raw Images Presentation

Adobe GoLive version 4.01 (http://www.adobe.com/products/golive/main.html) was used to create a Website integrating different modules (MRI data, annotated atlas images, and the 3D model of the 13.5 dpc embryo). For each embryonic stage, transverse, horizontal, and sagittal MR images are displayed as QuickTime movies (Apple Computer Inc.; http://www.apple.com/quicktime/). They are also provided as TIFF stacks that can be sliced in any

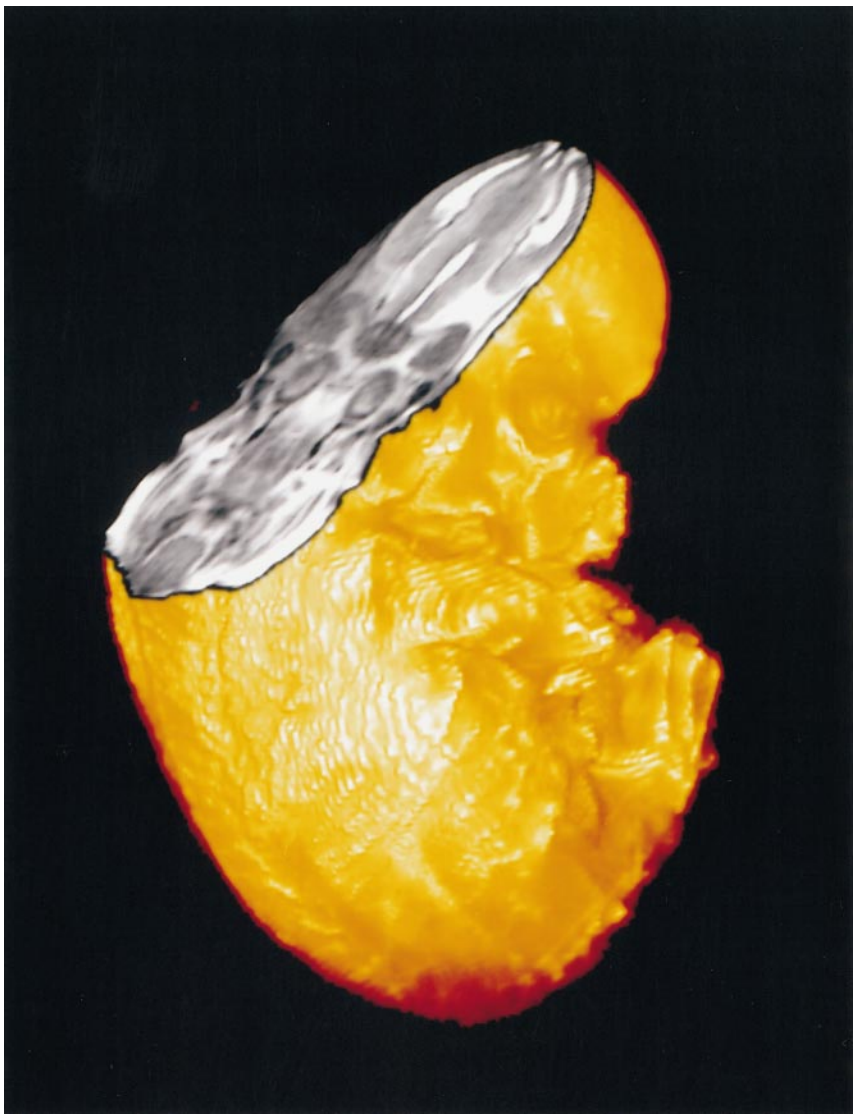

FIG. 1. Matching histological sections with μMR data. The slice plane of the model was established by virtually slicing the MRI data sets to match the section plane of the experimental histological sections. Once matched, the slicing angle was applied to the model.

direction or angle using shareware such as Brain Image (http://www.cap.stanford.edu/research/) or MacCube View (http://www.escape.ca/~physics/).

Delineating Anatomical Structures

Anatomical structures were manually delineated on individual MRI sections using Adobe Illustrator 8.01 (http://www.adobe.com/products/illustrator/main.html). Nomenclature and identification of structures were based principally on the atlas by Kaufman (Kaufman, 1994), but also on other atlases (Foster, 1998; Jacobowitz and Abbott, 1998; Schambra *et al.*, 1992; Theiler, 1989). In most instances, the boundaries between tissues were obvious. However, for some structures, the boundaries were not easily identifiable. In these cases, as is commonly done for atlas annotation purposes (Brune *et al.*, 1999), boundaries were placed according to the following criteria: (1) 3D morphology (organization of the structure as visible on adjacent and orthogonal slices); (2) position of surrounding tissues; (3) comparison with position of the structure in existing histological atlases (Foster, 1998; Jacobowitz and Abbott, 1998; Kaufman, 1994; Schambra *et al.*, 1992; Theiler, 1989). Some structures, such as the intestines, could not be fully segmented because the organ could not be identified in its entirety. Only structures and portions of structures that could be definitively identified were included in the model.

Annotated Atlas of a 13.5 dpc Mouse Embryo

To create a 2D annotated atlas of the 13.5 dpc mouse, we used transverse sections from an MRI data set recorded with $T_R = 1750$

FIG. 2. Steps used to "paint" the Dlx5/Dlx6 expression pattern into the brain model. (A) Histological sections (100 μm) displaying Dlx5/Dlx6 expression were (B) traced: blue represents Dlx5/6 expression; yellow, brain tissue; and red, ventricle borders. (C) The brain model slices corresponding with the plane of the histological section were extracted from the volume (Fig. 1) and the expression pattern "painted" into the model slices using borders as landmarks.

ms and T_E = 75 ms. This age embryo was chosen because the number of discernable anatomical structures is significant, but not excessively large (Kaufman, 1994) and because the MRI data have a high contrast-to-noise ratio for cerebral structures. Every fifth slice was segmented. We used the MetaMAP object-indexing technology [Eolas Technologies (http://www.eolas.net/aboutus.htm)] to annotate the atlas. Each outlined structure is linked to a descriptive text file via a 24-bit color index [8 bits per red/green/blue (RGB) channel]. Briefly, each segmented structure is assigned its own color (RGB value). The colors for each structure are mapped onto a hidden secondary image. Each color is linked to a descriptive file. Selecting a pixel on the primary image, via a mouse click, sends the pixel's coordinate to the color map by means of zMap, a Java applet (Eolas Technologies). The color index at that location is read and the appropriate descriptive file is called and displayed on the Web browser.

Generation of 3D Surface Models

To create 3D surface models, structures in the MRI sections were outlined in one of the three orthogonal directions (transverse, horizontal, or sagittal). For each structure, the MRI data set with the best contrast between the structure and surrounding tissues was chosen to outline the structure. For example, the liver was outlined on sagittal images with T_R = 3900 ms and T_E = 33 ms, whereas the vertebrae were outlined on horizontal images with T_R = 1750 ms and T_E = 75 ms. Three-dimensional surface renderings of embryonic structures were generated using form·Z [auto·des·sys inc. (http://www.formz.com)]. The outlines used to define individual structures were imported into form·Z, spaced appropriately, and then organized by organ systems. Outlines were used to construct surface models composed of polygonal meshes. Mesh densities were adjusted for each object to reveal details in small structures, while keeping the number of polygons low for structures with little detail. For example, the marginal layer model was constructed at high mesh density because it has many fingerlike projections surrounding the spinal cord. The liver, however, could be modeled using a lower mesh density because the surface contains fewer fine details. The entire embryo was reconstructed by juxtaposing organs that had been outlined in sections with different orientations or experimental parameters. To visually distinguish individual objects, the resulting surfaces were "shaded" (i.e., color, material, transparency, and reflectivity attributes and, in some cases, texture maps were assigned to the polygonal surface models). Lighting parameters were added to aid in 3D visualization. QuickTime movies were generated using either form·Z RenderZone renderer or Electric Image Animation System (Play, Inc.). These techniques reveal the 3D geometry and spatial relationships between organ systems.

Entering Gene Expression Data

As an example of how different types of information can be incorporated into this atlas, we "painted" in the expression pattern of the homeobox genes Dlx5/Dlx6 involved in the regulation of forebrain development. The Dlx5/Dlx6 expression pattern was entered into the model in a manner very similar to the segmented anatomical data. The original gene patterns were extracted from 100-μm transverse histological sections of a 13 dpc (TS 21) mouse, generously provided by T. Stühmer (Zerucha *et al.*, 2000). The sections came from transgenic animals expressing a *lacZ* reporter gene driven by a transcriptional enhancer within the intergene region of the zebra fish dlx5/dlx6 genes. In these mice the *lacZ* expression is identical to that of the endogenous Dlx5/Dlx6 genes (Zerucha *et al.*, 2000). Brain and ventricle borders as well as Dlx5/Dlx6 expression patterns were manually delineated on the digitized histological sections as described above. The 3D MRI data set was virtually sliced at various angles using Display software (ftp.bic.mni.mcgill.ca), until slices that best fit the brain and ventricle borders delineated on the histological section were found. Figure 1 is an example of the method used to determine the best-fitting slice angle. Note, the image in Fig. 1 was generated using Amira software. This slicing angle was applied to our 3D model and "virtual" slices with the thickness of the histological slices were created in (form·Z) and exported to Adobe Illustrator. Figure 2 displays the section with the poorest fit between virtual and histological sections. Traces of the brain, ventricle borders, and gene expression patterns from the histological sections were overlaid onto the "virtual" slices. The traces outlining the brain and ventricles borders were manually deformed to fit the brain and

ventricle borders of the "virtual" sections. The gene expression patterns were deformed in a similar way to create gene expression patterns transformed to the geometry of the "virtual" slices. All the virtual slices with the transformed gene patterns were then exported into form·Z, surface models were constructed, and a 3D rendering was created from the surface models.

RESULTS

MR Imaging and Raw Images Presentation

High-resolution 3D images of 6 to 15.5 dpc (TS 8 to 24) fixed mouse embryos were recorded using magnetic resonance imaging. Sagittal and transverse sections from 7, 11.5, and 15.5 dpc embryos are shown in Fig. 3. Images of 6, 7, 9.5, 11.5, 13.5, and 15.5 dpc (TS 8, 10, 15, 19, 22, and 24, respectively) embryos are found on the Website (http://mouseatlas.caltech.edu) (see above). Images are presented as QuickTime (QT) movies of consecutive sections passing through the embryo in three orthogonal directions (transverse, horizontal, and sagittal). They are also presented as stacks of TIFF sections that may be sliced at arbitrary orientations or rendered as volumes by using software tools such as Brain Image (http://www.cap.stanford.edu/research/) or MacCube View (http://www.escape.ca/~physics/). One QT movie occupies approximately 3 megabytes and one stack of TIFF images about 15 megabytes. The presentation of all images recorded (four or five images with various echo times for each embryo) occupies approximately 720 megabytes. As a consequence, for each embryo, we present one set of selected movies and one TIFF stack. High-resolution image data used for segmentation are available upon request.

Image Segmentation and Annotated 2D Atlas of 13.5 dpc Embryo

Transverse sections of the anterior portion of a 3D data set of a 13.5 dpc mouse were manually segmented and annotated. Two data sets were collected from a single embryo using different imaging protocols to enhance contrast in different structures. For example, one imaging protocol produces good contrast for bone primordium (T_R = 1750 ms and T_E = 75 ms), while another produces good contrast for internal organs (T_R = 3900 ms and T_E = 33 ms). Figure 4 displays the different steps used to create the annotated images. The left panel (Fig. 4A) shows the MRI section data. Structures in each MRI section were outlined using Adobe Illustrator 8.01 (Fig. 4B, middle panel). Published atlases were used to confirm identification of structures (Kaufman, 1994). However, each technique produces an image based on a specific physical property of the sample being studied. The photographic plates in Kaufman's atlas provide boundaries not always present in the MR data. Similarly, MR can reveal boundaries that are not apparent with optical methods and are therefore not considered discrete anatomical objects. For example, with MRI it is possible to distinguish between necrotic and poorly perfused tissue after an ischemic insult (Calamante *et al.*, 1999).

Each anatomical structure was outlined and filled with a different color and the same color used for a given structure in each section in which it occurred. Thus, each anatomical structure has a unique triplet of 8-bit numbers (RGB color) with which it is associated. Conversely, each volume element in the data has not only one of these RGB values associated with it, but also the MRI intensity value. This RGB value serves as an index to information about the structure. The set of RGB values also makes an image. This image is used to link the displayed MRI data to the descriptive files. When a particular pixel on an MRI section is chosen, the RGB value associated with that pixel is referenced, and the description indexed by that RGB value is displayed. The right panel (Fig. 4C) is the hidden RGB image that links the image map to descriptive files. A total of 108 structures have been outlined, including much of the central nervous system, blood vessels, arteries, eyes, and extracerebral tissues. Each volume element in this atlas has three values with which it is associated: an MRI intensity, an RGB anatomical index, and a flag for Dlx5/Dlx6 occupancy (Fig. 2). Other types of information can be added as needed.

Three-Dimensional Reconstruction and Rendering

To create the 3D surface model, structures were outlined in 2D sections taken along the three orthogonal directions (transverse, horizontal, and sagittal) of the 3D data sets. Separate 3D renderings of each organ were constructed from the outlines. The entire embryo was then reconstructed by combining the 3D models of the various organs using the original sections and Kaufman's atlas (Kaufman, 1994) to obtain proper alignment. Small interpretative errors were introduced during the manual segmentation when adjacent organs were outlined on different sets of orthogonal slices (e.g., on transverse and sagittal sections) and during the combination of the various organs into the whole embryo 3D model. The cumulative effects resulted in some misregistration in the surface models. These problems may be mitigated using applications that handle segmentation of 3D data directly in three dimensions (Amira; http://amira.zib.de). In this software, the traces created during the segmentation in one orthogonal direction are directly reported in the other two orthogonal directions. This allows the user to perform the segmentation and track progress directly within a single 3D image file. Moreover, in this fashion the 3D reconstruction can be created on a global basis for the whole embryo rather than organ by organ.

Once created, the 3D models were shaded, lighted, and rendered to better visualize the 3D geometry of individual structures and spatial relationships between structures within the developing mouse. Figure 5 demonstrates that anatomical segmentation is used not only for identifying structures in two dimensions but also allows organ systems to be viewed independently or as user-selected groups. In

this initial version of our atlas, we linked descriptive text files of several cerebral structures with 3D rendered movie files. To demonstrate that other data types can be incorporated and displayed in our 3D model, we entered the Dlx5/Dlx6 gene expression pattern for this stage. These genes are involved in the regulation of forebrain development (Zerucha *et al.,* 2000). The expression pattern was entered into our model by "fitting" the patterns from histological sections into corresponding model slices (Fig. 2). Figure 6 shows stereo-pair volumetric renderings of the Dlx5/Dlx6 expression pattern within 13.5 dpc mouse brain. A movie of the expression pattern can be found on the CD-ROM and the Website (http://mouseatlas.caltech.edu).

Website

The digital atlas outlined here is presented in its current entirety on the Website. The raw data are provided in the form of QuickTime movies and TIFF images because they are widely used formats. At this time the annotations are restricted to the 2D slices presented. This has the advantage of being highly interactive. Future work will incorporate a 3D version of the annotated information in which users may select arbitrarily oriented slices. TIFF stacks of the MRI data may be downloaded and converted to formats viewable with commercially available 3D visualization applications (Amira, http://amira.zib.de; Voxel View, http://www.vitalimages.com/products/voxelview.shtml; or Display, http://www.bic.mni.mcgill.ca/software).

DISCUSSION

Imaging Techniques (Comparison of MRI with Histology)

Magnetic resonance imaging is exquisitely sensitive to soft tissue, thus making it ideal for *in vivo* and nondestructive *in vitro* imaging of anatomical structures. We show mouse embryo μMR images with an isotropic resolution up to 16 μm per isotropic voxel. The digital images were used to create a digital atlas of a portion of one embryo and to create a 3D model of the animal. Other studies have used histological methods to reconstruct 3D models of embryos. The samples were sliced into thin sections, stained, photographed, digitized, and then reconstructed back into three dimensions. The creation of 3D models with this method becomes more and more difficult for late-stage embryos because of the increasing number of sections to process. To date, only early-stage [up to 9 dpc (TS 14)] embryos have been processed with this method (Brune *et al.,* 1999). Unlike these methods, μMRI provides a nondestructive means to collect 3D anatomical data from optically opaque specimens. The different slices issued from MR imaging are intrinsically aligned, thereby making it straightforward to visualize 3D structures even in late-stage embryos. The drawback of the μMRI method is that the resolution is poorer than that in optical methods. For example, histological images used to create the 3D model of a 9 dpc embryo (Brune *et al.,* 1999) were recorded with voxel size of $1.36 \times 1.36 \times 7$ μm. In the present study, a resolution of 25 μm per isotropic voxel side was recorded for the 13.5 dpc embryo. Although it took a day and a half to acquire the data, this resolution is sufficient for organ differentiation within the embryos; even small organs such as the adrenal glands could be visualized and modeled.

Another important difference between the two methods is the origin of contrast in the image. With histological methods, a number of different types of stains may be employed on the same or nearby sections. With MRI, the "stains" reside in the intrinsic physical properties of tissues that modulate the MR signal. No chemical stains need be added and several contrast mechanisms that arise from microscopic variations in chemical and physical properties (e.g., T_1, T_2, diffusion) can be used consecutively to image the same sample (Jacobs *et al.,* 1999a). New MRI methods such as magnetization transfer imaging (Nitz and Reimer, 1999), chemical shift imaging (Guimaraes *et al.,* 1999), or imaging protocols with the introduction of novel contrast agents (Louie *et al.,* 2000) should increase the panel of contrast mechanisms that can be used in embryos. The strengths and weaknesses of the histological and MRI data collection techniques complement each other. Moreover, the combination of these methods with micro-computed tomography (microCT) (Graichen *et al.,* 1998), phase-contrast microCT (Beckmann *et al.,* 1997), microPET (Cherry *et al.,* 1997), and blockface imagery (Cannestra *et al.,* 1997) would provide a wealth of information about embryological development and enable interesting comparisons between the *in vivo* and *in vitro* situations.

Entering Other Types of Information into the Model

An important feature of the digital atlas is the ability to input other data types, such as gene expression patterns, into the anatomical models. We superimposed Dlx5/Dlx6 expression data derived from experimental histological sections onto our model and reconstructed the 3D distribution of these genes within the context of the 13.5 dpc mouse brain. The 3D rendering of gene expression patterns can be a useful tool for a better understanding of the spatial organization of gene expression. More important, because the model can be used to "paint" in information from experimental sources, it can be used as a framework to integrate 3D patterns revealed by various experimental methods that then can be linked to other databases and data sources.

Dlx5/Dlx6 gene expression was classified as simply "present" or "absent." The relative intensity of gene expression can also be included in a straightforward manner. This will provide for more subtle renderings of gene expression patterns. Here, we manually fitted the gene expression patterns from histological sections into the model slices. Automated warping techniques can be used to optimize

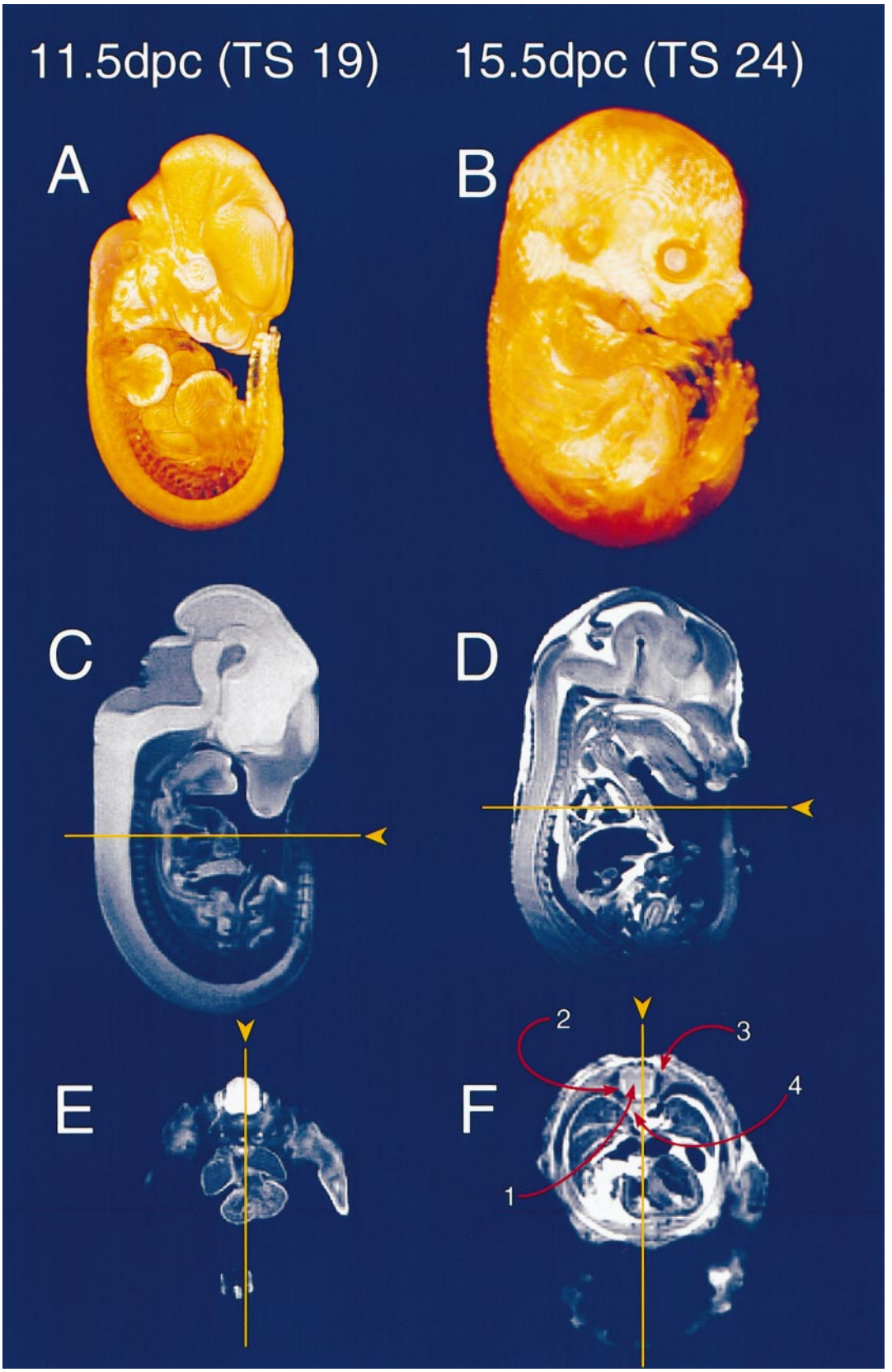

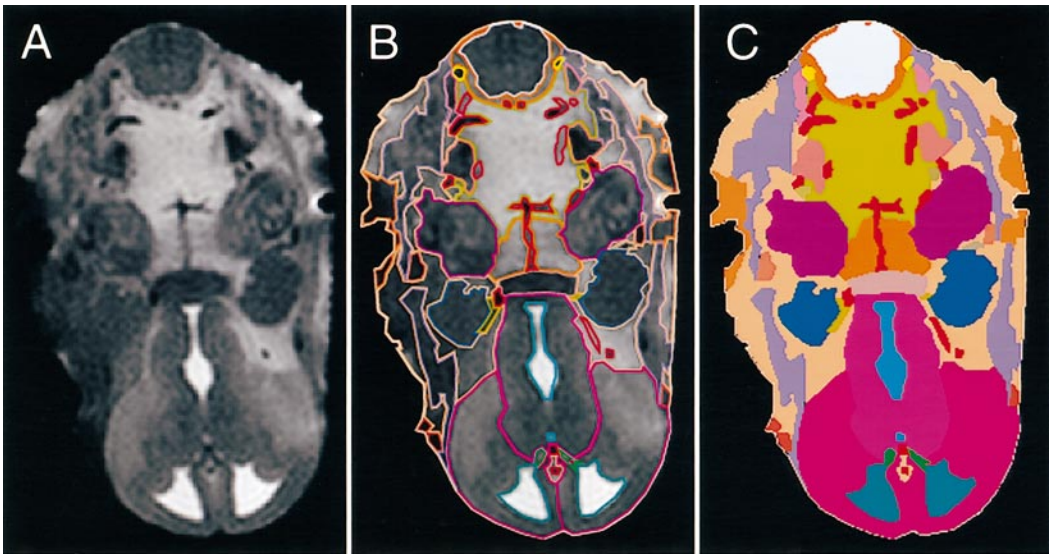

FIG. 4. Anatomical segmentation of 13.5 dpc embryo μMRI data. Transverse MRI sections (A) were used to delineate (segment) anatomical structures. (B) Each outlined structure was filled with an assigned 24-bit RGB color to produce a color map image shown in (C). The numerical value of the color in a particular pixel links that pixel to a descriptive text file. In practice, when a pixel is chosen in the MRI section (A) the RGB value assigned to that pixel (via C) is used to find the appropriate file that is then displayed.

incorporation of experimental information into the digital atlas (Van Essen *et al.*, 1998). The establishment of "fixed landmarks" will facilitate the digital mapping of other data types. We used the brain and ventricle borders as landmarks. These landmarks might not be optimal for incorporating information from sections of experimental embryos from various mouse strains with various brain sizes or when processing artifacts. One method we are exploring is to create a library of molecular landmarks that have known and invariant spatial relationships with anatomical structures. For example, Pax-3 in the chick is an early marker of placodes in the head (Baker *et al.*, 1999). Because the location of the placodes is well known, Pax-3 can be used as a landmark gene for orienting the experimental specimen and entering data into the models. Such a library can be used as a "warping map" for entering experimental data.

Finally, gene patterns in the present study were taken from 100-μm-thick sections and gene expression was inferred from the detection of a β-galactosidase marker gene. Sections of 100 μM thickness were used to provide sufficient β-galactosidase signal to be visualized. Visualization of endogenous genes will require other methods, such as *in situ* hybridization. With these methods, thinner sections are required for efficient staining, which dramatically increases the number of slices to be processed to create a 3D rendering of a given gene expression pattern. This is another reason to develop automatic outlining and warping protocols.

Conclusions

The atlas described here shares many features of the classic text-based histological atlas. It provides information in the form of slices where anatomical features are distinguishable because of their different physical characteristics. Anatomical features have been annotated, so that names are associated with structures. One can page through the various slices to get a better notion of the three-

FIG. 3. μMRI of fixed mouse embryos. Top row (A and B) shows volumetric representations of 11.5 and 15.5 dpc (TS 19 and 24, respectively) embryos. The surface of the embryos are clearly visible, allowing for the overall condition of the embryo to be assessed. (C and E) Transverse and sagittal sections of an 11.5 dpc specimen. T_R/T_E = 1000/5.5 ms, matrix = 512 × 256 × 256 points after zero-filling, (19.5 μm^3)/voxel. At this stage the limbs and vertebral elements are visible, although bone has not yet calcified. The forming heart, liver, and intestines are also apparent. (D and F) Transverse and sagittal sections of a 15.5 dpc specimen. By this stage the embryo is quite complex. The heart is well developed and the chambers easily distinguishable. In transverse section, the (1) spinal chord, (2) marginal layer (bright ring), (3) dorsal roots (lateral dark regions), and (4) vertebral body primordium are clearly visible and the lungs show complicated structure. T_R/T_E = 1750/100 ms, matrix = 512 × 256 × 256 points after zero-filling, (39 μm^3)/voxel.

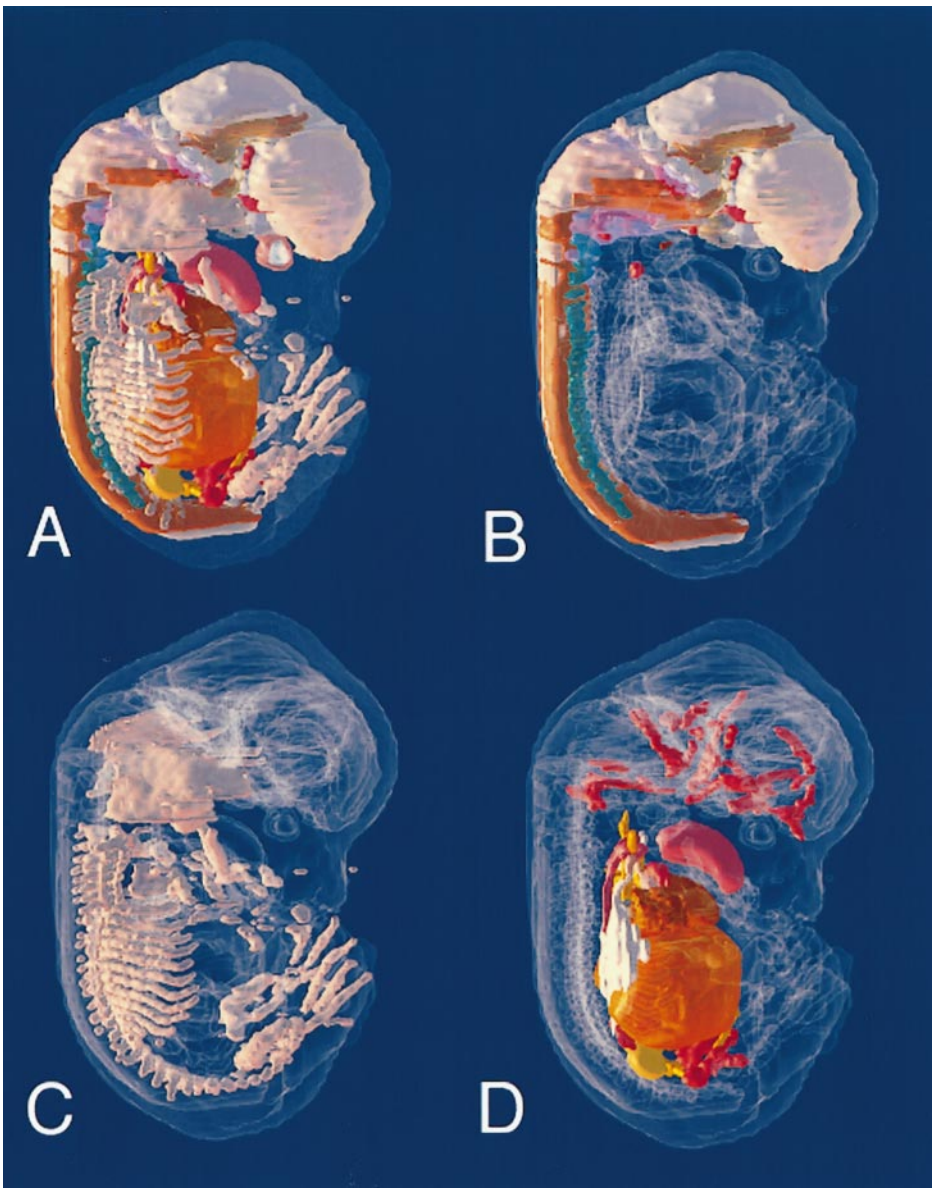

FIG. 5. 3D models derived from segmented data permit customizable views. The entire reconstructed embryo can be viewed with (A) all organ systems (except epidermis), (B) central nervous system, (C) skeletal system, or (D) any combinations of systems (in this case, enteric, pulmonary, circulatory, etc.) fully visible. Each structure is assigned a unique surface style to aid in visualization. For example in the CNS (B) the dorsal roots are blue/green, whereas the spinal cord is a pink/gray and the marginal layer orange. The cerebrum has been assigned some transparency to reveal the ventricles (purple) within. (D) The blood vessels in the brain and in the trunk are red, the kidneys are pink, the gonads are ochre, the lungs are white, and the heart is reddish brown.

dimensional nature of the specimen and the various parts of which it is comprised. Unlike the text-based atlas, the atlas presented here is digital, three-dimensional, and derived from magnetic resonance imaging data. The annotation is open-ended. We include a short description of identified structures, but the amount and kinds of information that can be included are essentially unlimited. The inclusion of other types of information from other sources is also straightforward; the example presented here is a relatively simple gene expression pattern derived from relatively thick histological slices. Annotation is in progress for images of mouse embryos at other time points included in the Webpage. We note that the noninvasive nature of the MRI experiments makes it feasible to perform repeated

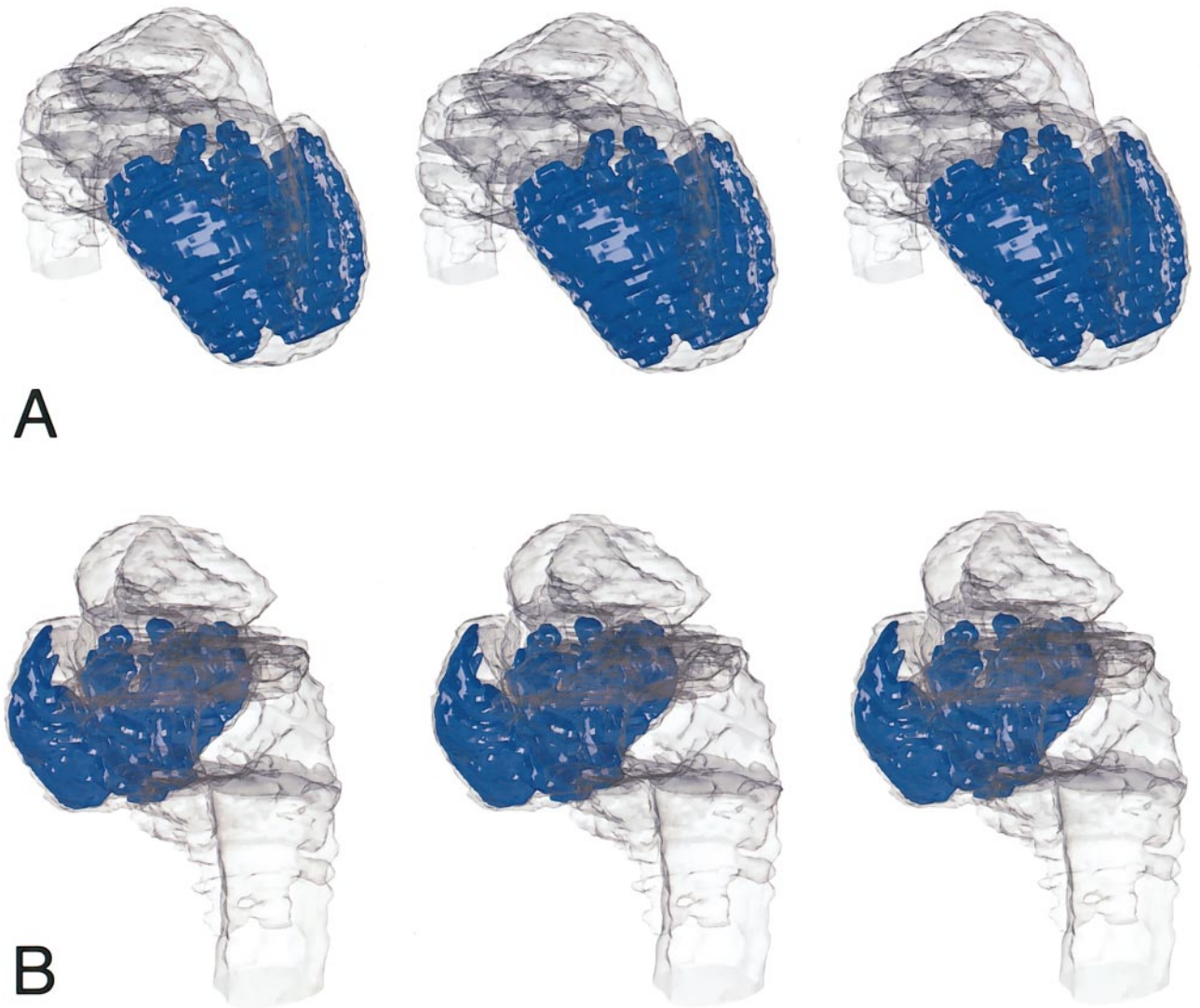

FIG. 6. Stereo-pair volumetric representations of forebrain expression of Dlx5/Dlx6 within the 3D brain model: (A) front view, (B) rear view. The left and middle images of each set are convergent stereo-pairs; the middle and right images are divergent stereo-pairs. Dlx5/Dlx6 are part of a cascade of gene expression involved in forebrain development (Zerucha *et al.*, 2000).

imaging of the same sample as it develops. Thus, an *in vivo* atlas of development of the mouse is a realistic goal.

A comprehensive understanding of the developmental process must include a global view of the developing system in space and time. Ultimately, digital atlases will allow a user to enter, search, and display different data types simultaneously and thus provide new ways of examining the relationships between the components within a developing system. These atlases will be powerful teaching tools, provide frameworks for organizing complex data, and allow visualization of intricate relationships among different types of information. This in-progress atlas is an early step in the creation of such tools.

APPENDIX: MAGNETIC RESONANCE IMAGING

Magnetic resonance imaging is not subject to the same limitations found in optical microscopy. This imaging technique can produce three-dimensional (3D) noninvasive images of optically opaque specimens. In the vast majority of experiments the image is based on the nuclear magnetic resonance (NMR) signal from the protons of water. In this short appendix, we provide a brief discussion of two areas of MRI that impinge directly on the analysis of the images presented in this work. For general background in MR

imaging there are a number of books, reviews, and Webpages describing MRI physics and its applications in biology (Andrew, 1990; Blackband *et al.*, 1999; Blumich and Kuhn, 1992; Callaghan, 1991a; Chen and Hoult, 1989; Kanal and Wehrli, 1986; Kuhn, 1990) (http://www.cis.rit.edu/htbooks/mri/).

Contrast in the Magnetic Resonance Image

The relative amount of MR signal arising from different regions (i.e., image contrast) is determined by spatial variations in physical and chemical properties of the sample. These include water concentration, chemical composition (fat versus water) (Dumoulin, 1985), temperature (Kuroda *et al.*, 1996), flow (Hofman *et al.*, 1995; Maki *et al.*, 1991; Xia and Callaghan, 1992), magnetic susceptibility (air versus tissue) (Grieve *et al.*, 2000; Skibbe *et al.*, 1995), and the underlying tissue microstructure (fiber tracts) (Ahrens *et al.*, 1998; Basser, 1995). Because many phenomena influence the MR signal the experimenter can modulate, to some extent, the image contrast through adjustment of the parameters that enter into the MR imaging scheme, by employing different schemes, or by the addition of contrast agents (Huber *et al.*, 1998; Jackson *et al.*, 1997; Jacobs *et al.*, 1999b; Lex, 1989). These physical characteristics affect water diffusion (D), proton spin-lattice relaxation times (T_1), and spin–spin relaxation times (T_2). T_1 is the characteristic time for a population of nuclei placed in a magnetic field to equilibrate along the field direction. T_2 is the characteristic time that individual nuclei contributing to the signal remain in phase with each other. At a magnetic field strength of 1.5 T in the human brain T_1 values for ventricular cerebrospinal fluid, white matter, and gray matter are ~4300, ~560, and ~1000 ms, respectively; T_2 values for white matter and gray matter are ~77 and ~80 ms, respectively (Bluml *et al.*, 1993; Steen *et al.*, 1994; Whittall *et al.*, 1999). T_1 values are somewhat shorter at 4 T (Kim *et al.*, 1994).

Adjectives such as "T_1-weighted," "T_2-weighted," and "diffusion-weighted" are applied to describe particular images obtained with particular experimental protocols. Typically, T_1-weighted images are collected with relatively short repetition times (T_R) (providing differential signal from species with differing T_1 relaxation times) and short echo times (T_E) (ensuring minimal signal modulation resulting from regional differences in T_2 relaxation times). In T_1-weighted images, regions with protons possessing long T_1 relaxation times will have relatively low intensity compared to those with short relaxation times. T_2-weighted images are collected with relatively long repetition times (ensuring minimal signal attenuation of species with long T_1 relaxation times) and long echo times (providing differential signal from species with differing T_2 relaxation times). In these types of images, areas with protons possessing long T_2 relaxation times will have relatively low intensity compared to those with short relaxation times. Diffusion-weighted data collection schemes (Le Bihan, 1995) have additional magnetic field gradients that cancel signals arising from molecules diffusing along the applied gradient direction(s). These types of experiments can be used to differentiate fiber tracts. Illustrations of how T_1 and T_2 weighting affect the resulting MR image are found at http://www.med.harvard.edu/AANLIB/cases/caseM/mr1_t/026.html. It must be remember that contrast in these "weighted" images is not solely from one source, but rather has been biased toward the desired source.

Spatial Resolution, Signal, and Noise in the Magnetic Resonance Image

One of the principal disadvantages of MRI is the intrinsically poor signal-to-noise ratio (SNR) of the experiment, made more severe by the small volumes of water contained within each volume element (voxel) of a microscopic image (Edelstein *et al.*, 1986; Lester *et al.*, 1999). This and other restrictions limit the spatial resolution obtainable with MRI. Factors contributing to the physical limits to spatial resolution in MRI have been discussed in detail by Callaghan (1991a) and others (Blumich and Kuhn, 1992; Cho *et al.*, 1988; House, 1984; Kuhn, 1990; Lauterbur, 1973; Zhou and Lauterbur, 1992). In addition to SNR, spatial resolution in biological samples is predominantly limited by line-width broadening and diffusion effects. Deterioration in resolution resulting from line-width effects can be compensated for by judicious choice of experimental conditions (e.g., bandwidth and gradient strength) that, in turn, influence the SNR of the resulting image (Callaghan, 1991a; Kuhn, 1990). Molecular diffusion has a number of effects in the MRI experiment (Le Bihan, 1991); besides being an important image contrast mechanism, diffusion also leads to signal attenuation and phase jitter. There are a number of ways of reducing the signal loss intrinsic to μMRI and thus achieving near-microscopic resolution. These include working at high magnetic fields and customizing hardware and software to the samples of interest (Narasimhan and Jacobs, 1996b). The success of these methods is evident from MR imaging experiments with spatial resolutions of 10 μm or less that have been achieved by several groups working at field strengths ranging from 4.7 to 14 T (Blumich and Kuhn, 1992). Estimates of the theoretical limits of resolution in the MR image range from 0.5 to 2 μm (Callaghan, 1991a; Cho *et al.*, 1988; Kuhn, 1990). In practice, such resolution extremes are rarely achieved as a result of limitations in the available SNR, which is limited by the amount of time available to acquire the image. Typically, the practical isotropic resolution for three-dimensional (3D) images yielding satisfactory SNR values is currently on the order of 20 μm for mouse-sized specimens.

ACKNOWLEDGMENTS

This work was funded in part by the Human Brain Project (DA08944) with contributions from the National Institute on Drug Abuse and the National Institute of Mental Health, the NCRR

(RR13625), and MH61223. M.D. was supported by the Bettencourt-Schueller foundation. S.R. was also supported by NRSA NS 11008-02. Anne Dhenain rendered able assistance in annotation work. We thank T. Stühmer and J. L. R. Rubenstein for their generous contribution of histological slices displaying Dlx5/Dlx6 expression patterns.

REFERENCES

Ahrens, E. T., Laidlaw, D. H., Readhead, C., Brosnan, C. F., Fraser, S. E., and Jacobs, R. E. (1998). MR microscopy of transgenic mice that spontaneously acquire experimental allergic encephalomyelitis. *Magn. Reson. Med.* **40,** 119–132.

Andrew, E. R. (1990). An introduction to nuclear magnetic resonance in biomedicine. *Can. Assoc. Radiol. J.* **41,** 2–7.

Baker, C. V., Stark, M. R., Marcelle, C., and Bronner-Fraser, M. (1999). Competence, specification and induction of Pax-3 in the trigeminal placode. *Development* **126,** 147–156.

Baldock, R. A. (1999). A three-dimensional model of the mouse at embryonic day 9. *Dev. Biol.* **216,** 457–468.

Basser, P. J. (1995). Inferring microstructural features and the physiological state of tissues from diffusion-weighted images. *NMR Biomed.* **8,** 333–344.

Beckmann, F., Bonse, U., Busch, F., and Gunnewig, O. (1997). X-ray microtomography (microCT) using phase contrast for the investigation of organic matter. *J. Comput. Assist. Tomogr.* **21,** 539–553.

Blackband, S. J., Buckley, D. L., Bui, J. D., and Phillips, M. I. (1999). NMR microscopy: Beginnings and new directions. *Magma* **9,** 112–116.

Blumich, B., and Kuhn, W. (1992). "Magnetic Resonance Microscopy," 604 pp. VCH Publishers, New York.

Bluml, S., Schad, L. R., Stepanow, B., and Lorenz, W. J. (1993). Spin-lattice relaxation-time measurement by means of a turbo-flash technique. *Magn. Reson. Med.* **30,** 289–295.

Bowtell, R. W., Peters, A., Sharp, J. C., Mansfield, P., Hsu, E. W., Aiken, N., Horsman, A., and Blackband, S. J. (1995). NMR microscopy of single neurons using spin-echo and line narrowed 2DFT imaging. *Magn. Reson. Med.* **33,** 790–794.

Brune, R. M., Bard, J. B. L., Dubreuil, C., Guest, E., Hill, W., Kaufman, M., Stark, M., Davidson, D., and Calamante, F., Lythgoe, M. F., Pell, G. S., Thomas, D. L., King, M. D., Busza, A. L., Sotak, C. H., Williams, S. R., Ordidge, R. J., and Gadian, D. G. (1999). Early changes in water diffusion, perfusion, T1, and T2 during focal cerebral ischemia in the rat studied at 8.5 T. *Magn. Reson. Med.* **41,** 479–485.

Callaghan, P. T. (1991). "Principles of Nuclear Magnetic Resonance Microscopy." Oxford Unversity Press, New York.

Cannestra, A. F., Santori, E. M., Holmes, C. J., and Toga, A. W. (1997). A three-dimensional multimodality brain map of the nemestrina monkey. *Brain Res. Bull.* **43,** 141–148.

Chen, C. N., and Hoult, D. I. (1989). "Biomedical Magnetic Resonance." Hilger, Bristol.

Cherry, S. R., Shao, Y., Silverman, R. W., Chatziioannou, A., Meadors, K., Siegel, S., Farquhar, T., Young, J., Jones, W. F., Newport, D., Moyers, C., Andreaco, M., Paulus, M., Binkley, D., Nutt, R., and Phelps, M. E. (1997). MicroPET: A high resolution PET scanner for imaging small animals. *IEEE Trans. Nucl. Sci.* **44,** 1161–1166.

Cho, Z. H., Ahn, C. B., Juh, S. C., Lee, H. K., Jacobs, R. E., Lee, S., Yi, J. H., and Jo, J. M. (1988). NMR microscopy with 4-μm resolution theoretical study and experimental results. *Med. Phys.* **15,** 815–824.

Dumoulin, C. L. (1985). A method for chemical shift selective imaging. *Magn. Reson. Med.* **2,** 583–585.

Durstewitz, D., Kroner, S., and Gunturkun, O. (1999). The dopaminergic innervation of the avian telencephalon. *Prog. Neurobiol.* **59,** 161–195.

Edelstein, W. A., Glover, G. H., Hardy, C. J., and Redington, R. W. (1986). The intrinsic signal-to-noise ratio in NMR imaging. *Magn. Reson. Med.* **3,** 604–618.

Farrar, T. C., and Becker, E. D. (1971). "Pulse and Fourier Transform NMR." Academic Press, New York.

Foster, G. A. (1998). "Chemical Neuroanatomy of the Prenatal Rat Brain." Oxford University Press, Oxford.

Fukushima, E., and Roeder, S. B. W. (1981). "Experimental Pulse NMR." Addison-Wesley, Reading, MA.

Gibaud, B., Garlatti, S., Barillot, C., and Aure, E. (1997). Methodology for the design of digital brain atlases. *Lect. Notes Artif. Intell.* **1211,** 441.

Graichen, H., Lochmuller, E. M., Wolf, E., Langkabel, B., Stammberger, T., Haubner, M., Renner-Muller, I., Englmeier, K. H., and Eckstein, F. (1998). A non-destructive technique for 3-D microstructural phenotypic characterisation of bones in genetically altered mice: Preliminary data in growth hormone transgenic animals and normal controls. *Anat. Embryol.* **199,** 239–248.

Grieve, S. M., Blamire, A. M., and Styles, P. (2000). The effect of bulk susceptibility on murine snapshot imaging at 7.0 T: A comparison of snapshot imaging techniques. *Magn. Reson. Med.* **43,** 747–755.

Guimaraes, A. R., Baker, J. R., Jenkins, B. G., Lee, P. L., Weisskoff, R. M., Rosen, B. R., and Gonzalez, R. G. (1999). Echoplanar chemical shift imaging. *Magn. Reson. Med.* **41,** 877–882.

Hofman, M. B., Visser, F. C., van Rossum, A. C., Vink, Q. M., Sprenger, M., and Westerhof, N. (1995). In vivo validation of magnetic resonance blood volume flow measurements with limited spatial resolution in small vessels. *Magn. Reson. Med.* **33,** 778–784.

House, W. V. (1984). NMR microscopy. *IEEE Trans. Nucl. Sci.* **NS-31,** 570–577.

Huber, M. M., Staubli, A. B., Kustedjo, K., Gray, M. H., Shih, J., Fraser, S. E., Jacobs, R. E., and Meade, T. J. (1998). Fluorescently detectable magnetic resonance imaging agents. *Bioconjug. Chem.* **9,** 242–249.

Jackson, E. F., Ginsberg, L. E., Schomer, D. F., and Leeds, N. E. (1997). A review of MRI pulse sequences and techniques in neuroimaging. *Surg. Neurol.* **47,** 185–199.

Jacobowitz, D. M., and Abbott, L. C. (1998). "Chemoarchitectonic Atlas of the Developing Mouse Brain." CRC Press, Boca Raton, FL.

Jacobs, R. E., Ahrens, E. T., Dickinson, M. E., and Laidlaw, D. (1999). Towards a microMRI atlas of mouse development. *Comput. Med. Imaging Graph.* **23,** 15–24.

Jacobs, R. E., Ahrens, E. T., Meade, T. J., and Fraser, S. E. (1999). Looking deeper into vertebrate development. *Trends Cell. Biol.* **9,** 73–76.

Jacobs, R. E., and Fraser, S. E. (1994). Magnetic resonance microscopy of embryonic cell lineages and movement. *Science* **263,** 681–684.

Johnson, G. A., Benveniste, H., Engelhardt, R. T., Qiu, H., and Hedlund, L. W. (1997). Magnetic resonance microscopy in basic

studies of brain structure and function. *Ann. NY Acad. Sci.* **820,** 139–148.

Kanal, E., and Wehrli, F. (1986). "Principles, Methodology and Applications of Biomedical Magnetic Resonance Imaging." VCH Publishers, New York.

Kaufman, M. H. (1994). "The Atlas of Mouse Development." Academic Press, London.

Kaufman, M. H., Brune, R. M., Baldock, R. A., Bard, J. B. L., and Davidson, D. (1997). Computer-aided 3-D reconstruction of serially sectioned mouse embryos: Its use in integrating anatomical organization. *Int. J. Dev. Biol.* **41,** 223–233.

Kaufman, M. H., Brune, R. M., Davidson, D. R., and Baldock, R. A. (1998). Computer-generated three-dimensional reconstructions of serially sectioned mouse embryos. *J. Anat.* **193,** 323–336.

Kim, S. G., Hu, X. P., and Ugurbil, K. (1994). Accurate T(1) determination from inversion-recovery images: Application to human brain at 4-Tesla. *Magn. Reson. Med.* **31,** 445–449.

Kuhn, W. (1990). NMR microscopy: Fundamentals, limits, and possible applications *Angew. Chem. Int. Ed. Engl.* **29,** 1–112.

Kuroda, K., Suzuki, Y., Ishihara, Y., and Okamoto, K. (1996). Temperature mapping using water proton chemical shift obtained with 3D-MRSI: Feasibility in vivo. *Magn. Reson. Med.* **35,** 20–29.

Lauterbur, P. C. (1973). Image formation by induced local interactions: Examples employing nuclear magnetic resonance. *Nature* **242,** 190.

Le Bihan, D. (1991). Molecular diffusion nuclear magnetic resonance imaging. *Magn. Reson. Q.* **7,** 1–30.

Le Bihan, D. (1995). "Diffusion and Perfusion Magnetic Resonance Imaging." Raven Press, New York.

Lester, D. S., Lyon, R. C., McGregor, G. N., Engelhardt, R. T., Schmued, L. C., Johnson, G. A., and Johannessen, J. N. (1999). 3-Dimensional visualization of lesions in rat brain using magnetic resonance imaging microscopy. *Neuroreport* **10,** 737–741.

Lex, L. (1989). Development of contrast enhancing agents in magnetic resonance imaging. *Acta Biochim. Biophys. Hung.* **24,** 265–281.

Louie, A. Y., Huber, M. M., Ahrens, E. T., Rothbacher, U., Moats, R., Jacobs, R. E., Fraser, S. E., and Meade, T. J. (2000). In vivo visualization of gene expression using magnetic resonance imaging. *Nat. Biotech.* **18,** 321–325.

Maki, J. H., MacFall, J. R., and Johnson, G. A. (1991). The use of gradient flow compensation to separate diffusion and microcirculatory flow in MRI. *Magn. Reson. Med.* **17,** 95–107.

Narasimhan, P. T., Ghosh, P., Fraser, S. E., and Jacobs, R. E. (1994). Magnetic-resonance microscopy: Challenges in biological imaging using a 500 MHz NMR microscope. *Proc. Indian AS–Chem. Sci.* **106,** 1625–1641.

Narasimhan, R. T., and Jacobs, R. E. (1996). Neuroanatomical micromagnetic resonance imaging. *In* "Brain Mapping: The Methods" (A. W. Toga and J. C. Mazziotta, Eds.), pp. 147–167. Academic Press, New York.

Nitz, W. R., and Reimer, P. (1999). Contrast mechanisms in MR imaging. *Eur. Radiol.* **9,** 1032–1046.

Palermo-Neto, J. (1997). Dopaminergic systems. Dopamine receptors. *Psychiatr. Clin. North Am.* **20,** 705–721.

Ringwald, M., Eppig, J., Kadin, J., and Richardson, J. (2000). GXD: A gene expression database for the laboratory mouse: Current status and recent enhancements. *Nucleic Acids Res.* **28,** 115–119.

Ringwald, M., Mangan, M., Eppig, J., Kadin, J., and Richardson, J. (1999). GXD: A gene expression database for the laboratory mouse. *Nucleic Acids Res.* **27,** 106–112.

Schambra, U. B., Lauder, J. M., and Silver, J. (1992). "Atlas of the Prenatal Mouse Brain." Academic Press, San Diego.

Skibbe, U., Christeller, J. T., Eccles, C. D., Laing, W. A., and Callaghan, P. T. (1995). A method to distinguish between chemical shift and susceptibility effects in NMR microscopy and its application to insect larvae. *Magn. Reson. Imaging* **13,** 471–479.

Smith, B. R., Shattuck, M. D., Hedlund, L. W., and Johnson, G. A. (1998). Time-course imaging of rat embryos in utero with magnetic resonance microscopy. *Magn. Reson. Med.* **39,** 673–677.

Steen, R. G., Gronemeyer, S. A., Kingsley, P. B., Reddick, W. E., Langston, J. S., and Taylor, J. S. (1994). Precise and accurate measurement of proton-T1 in human brain in vivo: Validation and preliminary clinical-application. *J. Magn. Reson. Imaging* **4,** 681–691.

Theiler, K. (1989). "The House Mouse: Atlas of Embryonic Development." Springer-Verlag, New York.

Toga, A. W. (1998). "Brain Warping." Academic Press, New York.

Toga, A. W., Ambach, K. L., Quinn, B., Shankar, K., and Schluender, S. (1996). Post-mortem anatomy. *In* "Brain Mapping: The Methods" (A. W. Toga and J. C. Mazziotta, Eds.), pp. 169–190. Academic Press, New York.

Toga, A. W., Santori, E. M., Hazani, R., and Ambach, K. (1995). A 3D digital map of rat brain. *Brain Res. Bull.* **38,** 77.

Toh, M. Y., Falk, R. B., and Main, J. S. (1996). Interactive brain atlas with the visible human project data: Development methods and techniques. *Radiographics* **16,** 1201–1206.

Van Essen, D. C., Drury, H. A., Joshi, S., and Miller, M. I. (1998). Functional and structural mapping of human cerebral cortex: Solutions are in the surfaces. *Proc. Natl. Acad. Sci. USA* **95,** 788–95.

Whittall, K. P., MacKay, A. L., and Li, D. K. B. (1999). Are mono-exponential fits to a few echoes sufficient to determine T-2 relaxation for in vivo human brain? *Magn. Reson. Med.* **41,** 1255–1257.

Williams, B. S., and Doyle, M. D. (1996). An internet atlas of mouse development. *Comput. Med. Imaging Graph.* **20,** 433–447.

Xia, Y., and Callaghan, P. T. (1992). One-shot velocity microscopy: NMR imaging of motion using a single phase-encoding step. *Magn. Reson. Med.* **23,** 138–153.

Zerucha, T., Stuhmer, T., Hatch, G., Park, B. K., Long, Q. M., Yu, G. Y., Gambarotta, A., Schultz, J. R., Rubenstein, J. L. R., and Ekker, M. (2000). A highly conserved enhancer in the Dlx5/Dlx6 intergenic region is the site of cross-regulatory interactions between Dlx genes in the embryonic forebrain. *J. Neurosci.* **20,** 709–721.

Zhou, X., and Lauterbur, P. C. (1992). NMR microscopy using projection reconstruction. *In* "Magnetic Resonance Microscopy" (B. Blumich and W. Kuhn, Eds.), pp. 3–27. VCH Publishers, New York.

Received for publication September 19, 2000
Revised January 4, 2001
Accepted January 4, 2001
Published online March 13, 2001